Computational Materials Science 254 (2025) 113911

Contents lists available at ScienceDirect

Computational Materials Science

journal homepage: www.elsevier.com/locate/commatsci

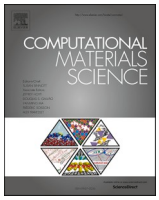

Full Length Article

Effects of strain rate, temperature, and defects on mechanical properties of xgraphene: Molecular dynamics study

Qing Peng [a,b,c,*], Ao Li [b], Gen Chen [b,d,e], Zeyu Huang [b,d,e], Xue Chen [b], Xintian Cai [f,g,*], Zhongwei Hu [d,e], Xiao-Jia Chen [a,*]

[a] School of Science, Harbin Institute of Technology, Shenzhen 518055, China
[b] State Key Laboratory of Nonlinear Mechanics, Institute of Mechanics, Chinese Academy of Sciences, Beijing 100190, China
[c] Guangdong Aerospace Research Academy, Guangzhou 511458, China
[d] Institute of Manufacturing Engineering, Huaqiao University, Xiamen 361021, China
[e] Institute of Mechanical Engineering and Automation, Huaqiao University, Xiamen 361021, China
[f] Laser Group, School of Mechanical Engineering, Hubei University of Technology, Wuhan 430068, China
[g] School of Mechanical Engineering, Hubei University of Technology, Wuhan 430068, China

ARTICLE INFO

Keywords:
Xgraphene
Mechanical properties
Molecular dynamics
Defects

ABSTRACT

Xgraphene is a newly proposed derivative of the graphene structure based on first-principles calculations. It is composed of 5–6-7 carbon rings, exhibits unique electrical characteristics, and is projected to be widely employed in high-performance metal-ion battery anodes. In this study, the mechanical properties of xgraphene were systematically evaluated through molecular dynamics simulations, considering factors such as size, strain rate, temperature, and defects, including vacancies, rectangular cracks, and circular voids. Our results demonstrate that xgraphene exhibits anisotropic mechanical behavior, with the armchair direction exhibiting a Young's modulus 1.0 % higher than the zigzag direction, indicating superior stiffness. The reliability of tensile simulations is influenced by size and strain rate. Variations in temperature, ranging from 1 K to 900 K, lead to reductions in Young's modulus by 6.4 % along the zigzag and armchair directions. Introducing vacancy defects from 0 to 3 % reduces Young's modulus by 22 % in the zigzag direction and 20 % in the armchair direction. Increasing the length of rectangular defects from 0 to 4 nm results in a 4.9 % decrease in Young's modulus along the zigzag and armchair directions. Similarly, increasing the diameter of circular defects from 0 to 4 nm reduces Young's modulus by 5.4 % along the zigzag direction and 5.3 % along the armchair direction. At later stages of fracture, xgraphene transitions to an amorphous state during tensile strain. This research provides a comprehensive understanding of xgraphene's mechanical behavior and offers a theoretical basis for its future applications.

1. Introduction

Graphene's unusual structure and exceptional physical qualities have drawn interest since its first discovery in 2004 [1]. As a two-dimensional crystal monolayer composed of carbon atoms, its structure is arranged in a hexagonal honeycomb shape, and it is one of the thinnest, hardest, and most conductive materials known [2–4]. The unusual structure of graphene provides a range of outstanding properties, including remarkable mechanical strength, exceptional flexibility, high electron mobility, a large specific surface area, and superior thermal conductivity [4–7]. These qualities make graphene show a wide range of application possibilities in electronic devices, energy storage, sensing technology, medical devices, and other fields [8–19]. Given its excellent mechanical properties, graphene's behavior under mechanical stress has become a central topic of research. Molecular dynamics (MD) techniques have been extensively applied recently in the investigation of graphene and its derivatives [20–33].

Xgraphene is a new two-dimensional form of carbon that has a rebuilt structure from graphene and is made up of pentagonal, hexagonal, and heptagonal carbon rings. With first-principles calculations, Wang et al. verified the mechanical, thermodynamic, and dynamic stability of xgraphene. Compared to most two-dimensional carbon allotropes, xgraphene has a lower energy and inherent metallic properties. Research on its electronic properties suggests that xgraphene holds

* Corresponding authors at: School of Science, Harbin Institute of Technology, Shenzhen 518055, China (Q. Peng). Laser Group, School of Mechanical Engineering, Hubei University of Technology, Wuhan 430068, China (X. Cai).
E-mail addresses: pengqing@imech.ac.cn (Q. Peng), caixintian@hbut.edu.cn (X. Cai), xjchen@hit.edu.cn (X.-J. Chen).

https://doi.org/10.1016/j.commatsci.2025.113911
Received 9 August 2024; Received in revised form 8 February 2025; Accepted 16 April 2025
Available online 19 April 2025

promise as a broad-spectrum anode material for metal-ion batteries (MIB), offering a new perspective for low-cost batteries [34].

Though several studies have investigated the electrical characteristics and stability of xgraphene, the mechanical aspects of the material remain quite lacking in systematic research. Mechanical property research is essential to encourage the use of xgraphene's fantastic physical and chemical features in an expanding range of applications in various situations. Thus, the primary objective of this study is to systematically explore the mechanical properties of xgraphene using MD simulations. Specifically, we examine the influence of key factors, such as size, strain rate, temperature, vacancy defects, and different types of defects, including rectangular and circular defects, as well as the material's anisotropy, on its mechanical response under diverse conditions.

The structure of the paper is the following: in the "Materials and Methods" section, we describe the simulation methods and setups; in the "Results and Discussion" section, we present and analyze the simulation results under different conditions, comparing our findings with existing research; and in the "Conclusions" section, we summarize the key findings and discuss the potential applications of xgraphene in materials science and nanotechnology.

2. Materials and methods

To investigate the mechanical properties of the xgraphene structure, we performed MD simulations using LAMMPS, which simulated the uniaxial tension. MD simulations, employed here as the primary computational method, utilize Newtonian mechanics to simulate atomic-scale material dynamics by numerically solving equations of motion. LAMMPS, a software adept at handling large-scale atomic systems, was chosen for its efficiency in simulating such dynamics [35]. Apart from that, xgraphene's original structure was built with the ATOMSK program, and OVITO software visualized and examined structural changes under tension. OVITO is a powerful material science visualization tool capable of various types of visualization for MD simulation data, including displaying changes in atomic positions and trajectories, plotting stress distribution, and calculating radial distribution functions [36]. These visualizations are critical for understanding xgraphene's deformation and fracture behavior during tension.

The structural features of xgraphene are depicted in Fig. 1. The material consists of two 5–6-7 rings per unit cell with 24 carbon atoms each. Xgraphene features "zigzag" edges along the x-axis and "armchair" edges along the y-axis direction, depending on the orientation of the hexagonal lattice. Like graphene, xgraphene is a single-layer material with a thickness of 0.334 nm. The lattice constants for the zigzag (x-axis) and armchair (y-axis) directions are a = 0.481 nm and b = 1.353 nm, respectively, with an interaxial angle of $\gamma = 90^{\circ}$. The C–C bond lengths range from 0.137 to 0.152 nm. For reliable simulation results, a model containing 26,880 carbon atoms was constructed. The dimensions of this model are 26.84 nm in length, 26.94 nm in width, and include a 10 nm vacuum layer along the z-axis, as shown in Fig. 1(c).

Periodic boundary conditions (p) were applied along the x and y axes, while free boundary conditions (f) were implemented along the z-axis. The system was simulated at the set temperature value with no external pressure.

The AIREBO/Morse potential function was used to describe the interactions between carbon atoms in xgraphene. This potential is a composite potential function that combines the REBO potential, the Lennard-Jones potential, and the torsion potential, and was introduced by O'Connor et al. to model interactions with more accurate long-range behavior [37]. This choice was informed by its relevance in studying the structure, mechanical properties, and chemical reactions of carbon materials. Based on literature and computational evidence, a cutoff distance of 0.2 nm was applied to C–C bonds to prevent strain hardening during rapid fracture [38–45].

The simulations used a 0.0001 ps time step to sufficiently capture atomic velocities and interaction time scales. We first stabilized the structure by performing energy minimization using the Conjugate Gradient (CG) technique. The energy minimization was performed with the following convergence criteria: an energy tolerance of 1×10^{-15} and a force tolerance of 1×10^{-15}, with a maximum of 10,000 iterations and function evaluations. Following this, the initial velocities of the system were set, and the temperature was adjusted to ensure the system reached thermodynamic equilibrium. In this step, we set the material's relaxation time to 40 ps and simulated it using the NPT ensemble. Strain was applied to the tension direction in uniaxial tension simulations using a strain rate set to 0.001/ps to prevent non-physical phenomena resulting from too high strain rates. During the tensile process, zero pressure was maintained perpendicular to the tension direction, and the temperature was kept constant.

Stress and strain data were computed and recorded in real-time using LAMMPS' built-in compute commands. Stress components were calculated for each atom, and variable commands were employed to calculate average stress and von Mises stress, with data recorded every 250 steps. The stress–strain curve was constructed from the collected data. Key mechanical properties, including ultimate stress (σ), ultimate strain (ε), Young's modulus (E), and toughness, were extracted from the curve. Ultimate stress refers to the maximum stress the material can withstand during tension, corresponding to the peak in the stress–strain curve. Ultimate strain refers to the strain value at which the material fractures during tension, i.e., the strain value corresponding to the ultimate stress. Young's modulus, a material's modulus of elasticity, is estimated from the linear region of the stress–strain curve, where the material exhibits elastic behavior. Toughness, represented by the area under the stress–-strain curve, quantifies the material's ability to absorb energy under tension. The coefficient of variation was calculated to assess the distribution and concentration of the mechanical properties above, with the standard deviation divided by the mean. A larger coefficient of variation indicates more distributed or varied data; a smaller coefficient suggests

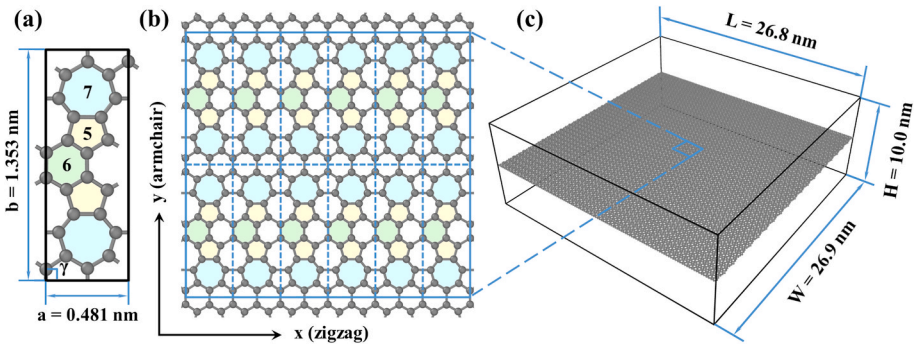

Fig. 1. Structural representation of xgraphene. (a) Primitive unit cell of xgraphene, composed of pentagonal, hexagonal, and heptagonal carbon rings. (b) Local view of a monolayer xgraphene. (c) Three-dimensional representation of xgraphene containing 26,880 carbon atoms.

more centralized or less varied data.

To assess the uncertainty and consistency of our results, we performed five independent simulations of xgraphene at 300 K in both zigzag and armchair directions with different configurations which are obtained from the same procedure but different relaxation times (40 ps, 50 ps, 60 ps, 70 ps, and 80 ps, respectively) from the same initial configuration. The stress–strain curves from these simulations are presented in Fig. 2. The standard deviation, average, and coefficient of variation for the ultimate stress and ultimate strain were calculated for both directions. In the zigzag direction, the standard deviation of ultimate stress was 1.016 GPa, with an average value of 63.14 GPa, and the coefficient of variation of ultimate stress was calculated to be 1.6 %. For ultimate strain, the standard deviation was 0.0023, with an average value of 0.092, and the coefficient of variation was 2.5 %. In the armchair direction, the standard deviation of ultimate stress was 0.936 GPa, with an average value of 75.27 GPa, and the coefficient of variation for ultimate stress was 1.2 %. For ultimate strain, the standard deviation was 0.0027, with an average value of 0.114, and the coefficient of variation was 2.4 %. These results demonstrate that while there are fluctuations in the mechanical properties, the observed variations are within acceptable limits (within 2.4 %) and reflect physical phenomena.

3. Results and Discussions

3.1. Size effect

MD simulation is based on statistical mechanics. For small systems, the statistical simulation results may be limited because there aren't many atoms, which makes it hard to predict the mechanical properties. Oversized systems can increase computational costs. Thus, including size effects in MD models is really essential and helps to maximize computational resources. Choosing appropriate model sizes ensures that simulation results accurately depict material behavior at relevant scales, thereby improving their authenticity and dependability.

In this study, we investigated four defect-free xgraphene models with sizes ranging from 6.73 nm × 6.71 nm to 53.87 nm × 53.68 nm. The model sizes increased by factors of four, with the number of atoms in the systems varying from 1,680 to 107,520. Uniaxial tension simulations were conducted along both the zigzag and armchair directions at 300 K to examine the size effects on the mechanical properties of xgraphene. The stress–strain curves, presented in Fig. 3, exhibit similar trends prior to fracture across all sizes, indicating that size has minimal impact on the Young's modulus. The coefficient of variation for Young's modulus was only 0.06 % along the zigzag direction and 0.1 % along the armchair direction. However, there are significant differences between ultimate strain and ultimate stress. As the number of atoms increased from 1,680 to 107,520 along the zigzag direction, ultimate stress decreased by 11 %, from 71.00 GPa to 63.24 GPa; ultimate strain decreased by 16 %, from 0.111 to 0.093. Along the armchair direction, ultimate stress decreased by 4.6 %, from 77.52 GPa to 73.97 GPa; ultimate strain decreased by 8.3 %, from 0.120 to 0.110.

For the smallest model containing 1,680 atoms, the ultimate stress–strain behavior showed the most noticeable differences during tensile testing along both directions. As the system size increased, the ultimate stress–strain curves began to converge. Along the zigzag direction, the curves nearly overlapped when the atom count reached 26,880 and 107,520. In the armchair direction, the curves exhibited minimal differences compared to larger models when the atom count reached 6,720. This trend indicates that as the size of the model increases, the simulation results become increasingly stable and consistent. Therefore, a model containing 26,880 atoms is considered sufficient for subsequent studies.

3.2. Strain rate effect

The strain rate refers to the rate at which strain changes in a material per unit of time. In MD simulations, selecting an appropriate strain rate is essential to accurately represent the material's real mechanical behavior. A too-low strain rate might provide too long simulation periods; a too-high strain rate could produce distorted simulation results. Therefore, choosing an optimal strain rate is crucial for reliable simulations.

In this study, uniaxial tensile simulations of defect-free xgraphene were performed at five different strain rates, spanning three orders of magnitude from 5×10^8/s to 5×10^{10}/s at 300 K. The resulting stress–strain curves, shown in Fig. 4, illustrate the strain rate exerts a substantial influence on the mechanical response of xgraphene along both the zigzag and armchair directions. As the strain rate increased from 5×10^8/s to 5×10^{10}/s, ultimate stress decreased from 74.68 GPa to 63.34 GPa along the zigzag direction, representing a decrease of 15 %; along the armchair direction, it decreased from 81.40 GPa to 73.42 GPa, representing a 9.8 % decline. Despite these reductions in ultimate stress, the stress–strain curves for different strain rates almost overlapped before fracture, indicating that strain rate has minimal influence on the Young's modulus. The coefficient of variation of Young's modulus was only 0.2 % in the zigzag direction and 0.03 % in the armchair direction. Higher strain rates are accompanied by increased ultimate strains and stresses, indicating increased ductility. Conversely, lower strain rates result in reduced ultimate stresses and smaller ultimate strains, indicating brittleness.

While the thermal effects inside the material may not be obvious, a higher strain rate results in an increase in kinetic energy inside the material and more activation of dislocation motion and slip, which improves the ductility and strength of the material. At lower strain rates, atoms and molecules have more time to exchange energy with their surroundings, allowing the system to achieve a more complete energy equilibrium. However, if the material is inherently brittle or prone to defects, these mechanisms may not be evident. Consequently, the low strain rate in this case makes defects and cracks more likely to propagate, resulting in lower stress and strain at break, exhibiting brittleness,

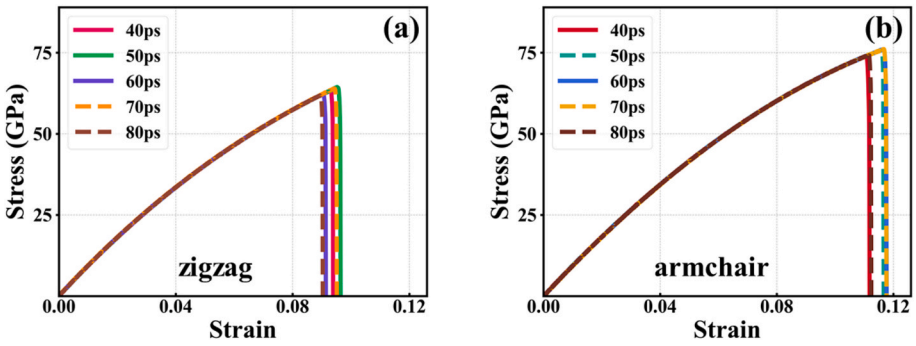

Fig. 2. Stress–strain curves of xgraphene at 300 K for different configurations that obtained from relaxation times (40 – 80 ps). (a) Stress–strain behavior along the zigzag direction. (b) Stress–strain behavior along the armchair direction.

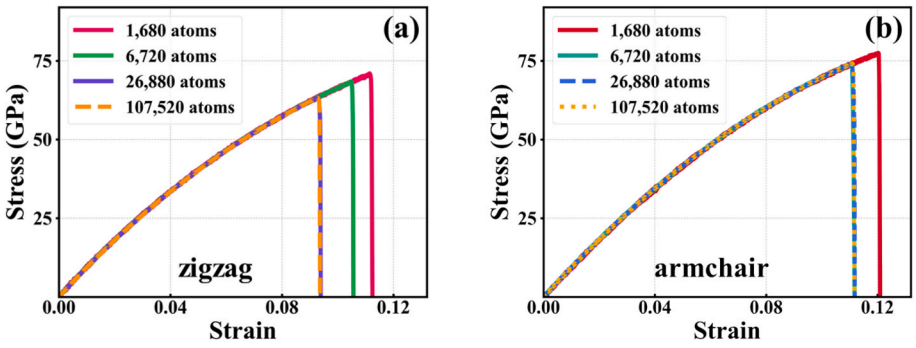

Fig. 3. Stress–strain curves of xgraphene at different sizes at 300 K. (a) Stress–strain response along the zigzag direction for various sample sizes. (b) Stress–strain response along the armchair direction for various sample sizes.

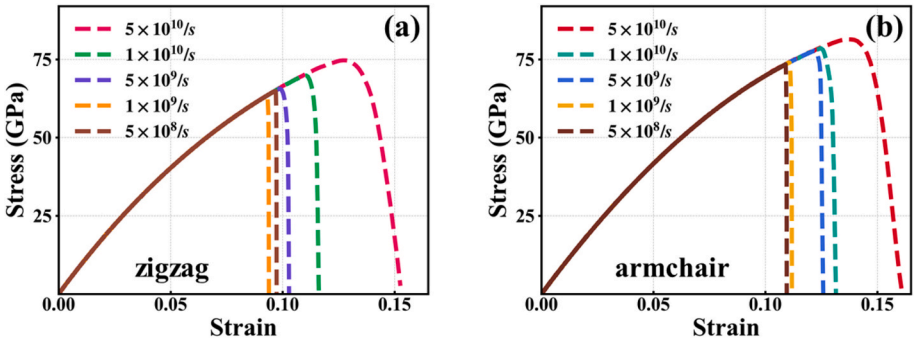

Fig. 4. Stress–strain curves of xgraphene for different strain rates at 300 K. (a) Stress–strain response along the zigzag direction for various strain rates. (b) Stress–strain response along the armchair direction for various strain rates.

conversely.

Interestingly, results at strain rates of 5×10^8/s and 1×10^9/s show minimal disparity: zigzag direction ultimate stress differs by 2.58 %, ultimate strain by 3.89 %; armchair direction ultimate stress differs by 0.74 %, ultimate strain by 1.33 %. These small variations suggest that the plastic deformation characteristics and yield strength of xgraphene are stable at these strain rates. Based on these results, and considering that the simulation time at 5×10^8/s is twice as long as that at 1×10^9/s,

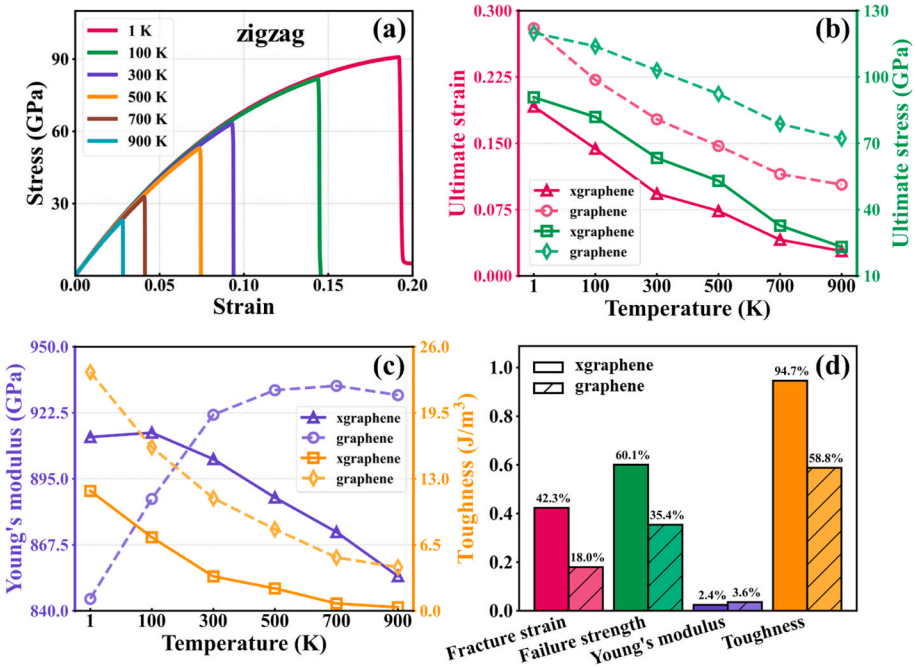

Fig. 5. Temperature effect on xgraphene's mechanical properties along the zigzag direction. (a) Stress–strain curves for xgraphene at various temperatures. (b, c) Variation of ultimate strain, ultimate stress, Young's modulus, and toughness of xgraphene and graphene as a function of temperature. (d) Coefficient of variation for the mechanical properties of xgraphene with temperature changes.

a strain rate of 1×10^9/s was selected for subsequent simulations to optimize computational efficiency.

3.3. Temperature effect

In practical applications, xgraphene may work as an anode for metal-ion batteries across a range of temperatures. Since temperature directly influences the thermal vibrations of atoms, it is essential to assess the effects of temperature on the mechanical behavior of xgraphene.

To evaluate the temperature dependence of xgraphene's mechanical properties, we performed uniaxial tensile simulations of defect-free xgraphene across six temperature ranges, from 1 K to 900 K. Figs. 5 and 6 display the stress–strain curves of xgraphene in the zigzag and armchair directions, respectively, along with calculations of ultimate stress, ultimate strain, Young's modulus, and toughness with temperature changes. The mechanical properties of xgraphene and graphene both decrease monotonically as the temperature rises, except for the Young's modulus of graphene. For graphene, the Young's modulus along the armchair direction increases from 845.0 GPa at 1 K to 933.7 GPa at 700 K, before slightly decreasing to 929.9 GPa at 900 K; along the zigzag direction, the Young's modulus of graphene rises from 969.2 GPa at 1 K to 990.2 GPa at 300 K, and then gradually decreases to 972.2 GPa at 900 K [46].

In Fig. 5, for uniaxial tension along the zigzag direction, the ultimate stress of xgraphene drops by 74 %, from 90.81 GPa at 1 K to 23.16 GPa at 900 K. The ultimate strain decreases by 85 %, from 0.192 to 0.028. Young's modulus decreases by 6.4 %, from 912.4 GPa to 854.4 GPa, and toughness decreases by 97 %, from 11.81 J/m^3 to 0.35 J/m^3. In contrast, graphene's ultimate stress declines by 40 %, from 119.98 GPa to 72.18 GPa, ultimate strain decreases by 63 %, from 0.280 to 0.103, and toughness diminishes by 82 %, from 23.50 J/m^3 to 4.29 J/m^3.

In Fig. 6, during armchair direction tensile strain, xgraphene's ultimate stress decreases by 57 %, from 91.16 GPa to 39.03 GPa. The ultimate strain decreases by 71 %, from 0.174 to 0.051. Young's modulus drops by 6.4 %, from 930.8 GPa to 871.2 GPa, and toughness decreases by 89 %, from 10.52 J/m^3 to 1.14 J/m^3. In comparison, graphene's ultimate stress decreases by 33 %, from 99.51 GPa to 66.42 GPa, ultimate strain decreases by 53 %, from 0.178 to 0.084, and toughness reduces by 74 %, from 12.10 J/m^3 to 3.13 J/m^3. These changes occur because the increased thermal vibrations of atoms in xgraphene at higher temperatures reduce the bond energies between atoms, making the material more susceptible to stretching or fracture under stress.

Overall, compared with the armchair direction, xgraphene exhibits greater sensitivity to temperature variations along the zigzag direction. Temperature significantly impacts the mechanical properties of xgraphene, where mechanical performance uniformly declines with increasing temperature [46,47].

3.4. The vacancy defects effect

In an ideal crystalline material, atoms are arranged periodically. However, in real materials, various complex phenomena lead to deviations from the ideal lattice structure. During the preparation and application of materials, defects such as vacancies are inevitable in xgraphene. These defects significantly affect the material's physical properties, including electrical conductivity, thermal conductivity, and mechanical behavior [40,42,48–55].

Vacancy defects are common in crystalline materials and occur when atoms or ions are missing from their lattice positions [56,57]. Increased brittleness and decreased fatigue resistance may result from these defects, which may occur during material processing or usage. Understanding and controlling the emergence and distribution of vacancy defects occupies a fundamental position in material engineering, as it can enhance certain material properties. For example, in semiconductor materials, vacancy defects are intentionally introduced to modulate the material's electronic properties for device manufacturing. Thus, understanding the role of vacancy defects is essential in both materials science and engineering, as well as for assessing material performance in practical applications [11,12,58].

Vacancy formation energy (E_v) is an important property. It refers to the amount of energy required to break the chemical bond between a crystal lattice's atom or ion and the surrounding atom or ion and move that atom to infinity. The vacancy formation energy is an important physical quantity to evaluate the difficulty of forming vacancy defects in

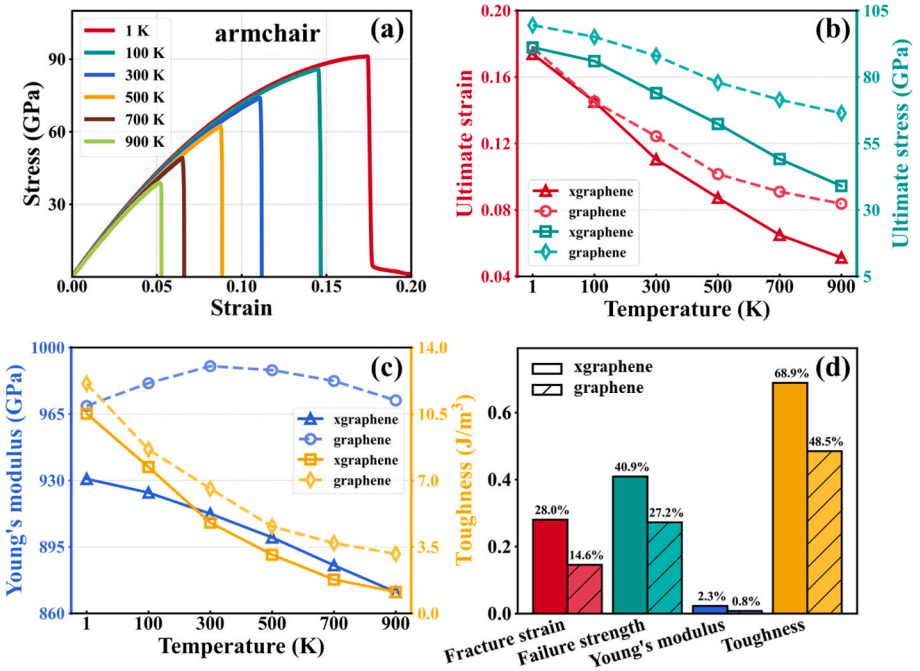

Fig. 6. Temperature effect on xgraphene's mechanical properties along the armchair direction. (a) Stress–strain curves for xgraphene at various temperatures. (b, c) Variation of ultimate strain, ultimate stress, Young's modulus, and toughness of xgraphene and graphene as a function of temperature. (d) Coefficient of variation for the mechanical properties of xgraphene with temperature changes.

the crystal. The equation used to calculate the energy E_v is:

$$E_v = E_f - (\frac{N_0 - 1}{N_0}) \cdot E_i \quad (1)$$

where N_0 is the initial number of atoms in the system, E_f is the total energy of the system after the removal of the atom, and E_i is the total energy of the system before the removal.

In this study, the vacancy formation energies of 24 atoms in the unit cell using a xgraphene system of 26,880 carbon atoms were calculated by MD simulations. It was found that 24 atoms could be divided into four groups by different values to form energy with vacancies. As shown in Fig. 7, we numbered the 24 atoms and divided them into different groups by color. The vacancy formation energy is shown as follows: from small to large, numbered 3, 4, 9, 10, 15, 16, 21, 22, that is, the atomic vacancy formation energy marked in red is 5.793 eV; the numbers are 1, 14, 18, 19, that is, the atomic vacancy formation energy marked yellow is 5.832 eV; the numbers are 2, 5, 8, 11, 13, 17, 20, 23, that is, the atomic vacancy formation energy marked in green is 6.028 eV; and the numbers are 6, 7, 12, 24, i.e., the atomic vacancy formation energy marked in blue is 7.158 eV. For comparative analysis, we also calculated the vacancy formation energies of the four atoms in the graphene unit cell; that is, the vacancy formation energies of the dark blue atoms are all 7.188 eV.

A lower vacancy formation energy means that there is a lower energy barrier to vacancy formation, so the red atom group with a lower vacancy formation energy is more likely to form a vacancy in the crystal lattice than the blue group, thus promoting crack propagation and strain concentration during the tensile process of the material. Notably, the vacancy formation energy in xgraphene is generally lower than that in graphene, suggesting that xgraphene is more prone to defect formation in practical applications.

To further investigate the effect of vacancy defects on the mechanical properties of xgraphene, we introduced varying concentrations of vacancy defects by randomly removing 0.1 %, 0.5 %, 1 %, 1.5 %, 2 %, 2.5 %, and 3 % of the atoms from a system containing 26,880 carbon atoms. The stress–strain curves obtained from uniaxial tensile simulations along the zigzag and armchair directions, shown in Figs. 8 and 9, illustrate the mechanical degradation caused by the increasing vacancy defect concentration, comparing parameters to the defect-free xgraphene and graphene.

As the vacancy defect concentration increased, mechanical parameters above generally exhibited a decreasing trend compared to defect-free xgraphene. As shown in Fig. 8, when vacancy defect concentration increases from 0 % to 3 % along the zigzag direction, xgraphene's ultimate stress decreases from 63.34 GPa to 13.98 GPa, marking a 78 % reduction; ultimate strain decreases from 0.093 to 0.019, a decrease of 80 %; Young's modulus decreases from 903.2 GPa to 702.6 GPa, a 22 % reduction; and toughness decreases from 3.39 J/m^3 to 0.38 J/m^3, an 89 % decrease. In contrast, graphene's ultimate stress decreases from 103.00 GPa to 46.34 GPa, a 55 % reduction; ultimate strain decreases from 0.177 to 0.070, a 60 % decrease; Young's modulus decreases from 921.7 GPa to 750.6 GPa, a 19 % reduction; and toughness decreases from 11.08 J/m^3 to 1.82 J/m^3, an 84 % reduction.

As depicted in Fig. 9, along the armchair direction, xgraphene's ultimate stress decreases from 73.97 GPa to 33.63 GPa, a 55 % reduction; ultimate strain decreases from 0.110 to 0.050, a 55 % decrease; Young's modulus decreases from 912.5 GPa to 732.8 GPa, a 20 % reduction; and toughness decreases from 4.78 J/m^3 to 0.97 J/m^3, an 80 % decrease. Meanwhile, graphene's ultimate stress decreases from 88.00 GPa to 41.01 GPa, a 53 % reduction; ultimate strain decreases from 0.124 to 0.055, a 56 % decrease; Young's modulus decreases from 990.2 GPa to 782.7 GPa, a 21 % reduction; and toughness decreases from 6.57 J/m^3 to 1.26 J/m^3, an 81 % reduction.

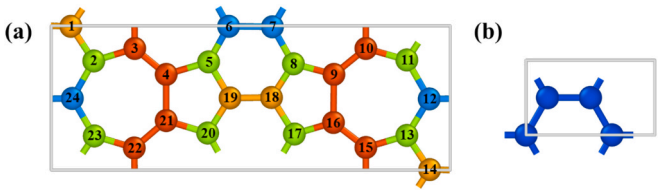

Fig. 7. Schematic of vacancy formation energy. (a) Xgraphene. (b) Graphene.

The introduction of vacancy defects becomes the occurrence point of cracks during the tensile process and accelerates crack propagation, resulting in an increase in the breakability of the material and the concentration of local strain, which affects the overall elastic performance of the material, which is manifested as an irregular stress–strain curve. As a result, the introduction of vacancy defects significantly affects the mechanical properties of xgraphene [59–68]. Apart from exhibiting smaller coefficients of variation in ultimate strain, Young's modulus, and toughness along the armchair direction compared to graphene, other parameters demonstrate greater sensitivity than graphene. Similar to temperature effects, vacancy defects are more influential along the zigzag direction compared to the armchair direction [69,70].

3.5. Defect size and shape effect

In practical applications, xgraphene can be subjected to various external factors, including chemical exposure and mechanical stress, etc., which can lead to the formation of defects, such as cracks and voids. These defects act as stress concentrators, significantly influencing the material's mechanical behavior. The size and shape of these defects play a critical role in determining both the direction and rate of crack propagation, which affects the overall mechanical properties of the material. Thus, it is essential to consider both the size and geometry of defects when studying the mechanical behavior of xgraphene.

In this study, we examine the effects of rectangular and circular defects of various sizes on xgraphene's mechanical characteristics. The results are presented in sections 3.5.1 and 3.5.2, where we simulate defects of different shapes and sizes. The von Mises stress distribution during tensile deformation is analyzed to visualize the stress concentration and fracture progression. The stress distribution, shown in Fig. 10, is represented by atomic colors corresponding to von Mises stress values, which highlight the material's internal stress evolution. Von Mises stress is an essential parameter for assessing yield strength and is critical in evaluating the safety and reliability of materials in engineering contexts. Each dataset includes four stages: the model after relaxation, just before fracture, during crack propagation, and during the transition to an amorphous state, with the appearance of a large red region signifying the onset of the amorphous phase. To further investigate the formation and transformation of the amorphous state during tensile deformation, we apply radial distribution function (RDF) analysis in Section 3.5.3.

3.5.1. Rectangular crack defects

We introduced rectangular crack defects perpendicular to the tensile direction at the center of the xgraphene model. The effects of four different crack lengths—1, 2, 3, and 4 nm, with a constant width of 1 nm—on the mechanical properties of xgraphene were examined. Uniaxial tensile simulations were performed in the directions of zigzag and armchair, and the results were compared with the defect-free xgraphene. Fig. 11 (a, b) display the stress–strain curves for xgraphene under tensile strain with rectangular cracks of varying lengths. Longer cracks exhibit lower strength and earlier fracture points.

As the crack lengths ranged from 0 to 4 nm, the following changes were observed: Along the zigzag direction, ultimate stress decreases from 63.34 GPa to 34.88 GPa, marking a 45 % reduction; ultimate strain decreases from 0.093 to 0.044, a decrease of 53 %; Young's modulus decreases from 903.2 GPa to 859.2 GPa, a 4.9 % reduction; and toughness decreases from 3.39 J/m^3 to 0.88 J/m^3, a 74 % decrease. Along the

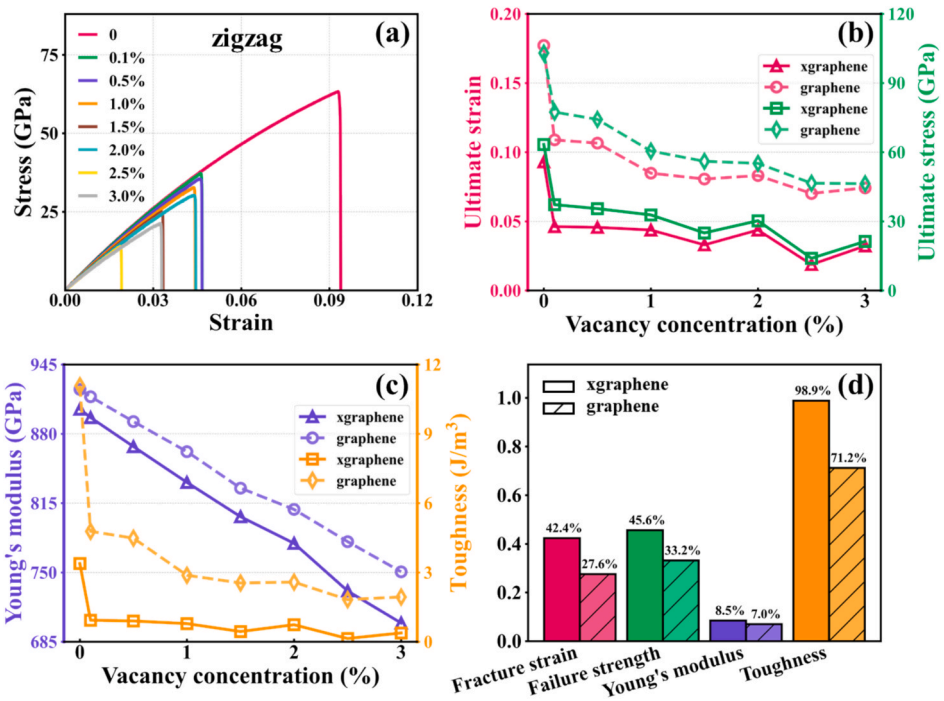

Fig. 8. The vacancy defects effect on xgraphene's mechanical properties along the zigzag direction. (a) Stress–strain curves for xgraphene at different vacancy concentrations. (b, c) Variation of ultimate strain, ultimate stress, Young's modulus, and toughness with increasing random vacancy concentrations for xgraphene and graphene. (d) Coefficient of variation for the mechanical properties of xgraphene with varying random vacancy concentrations.

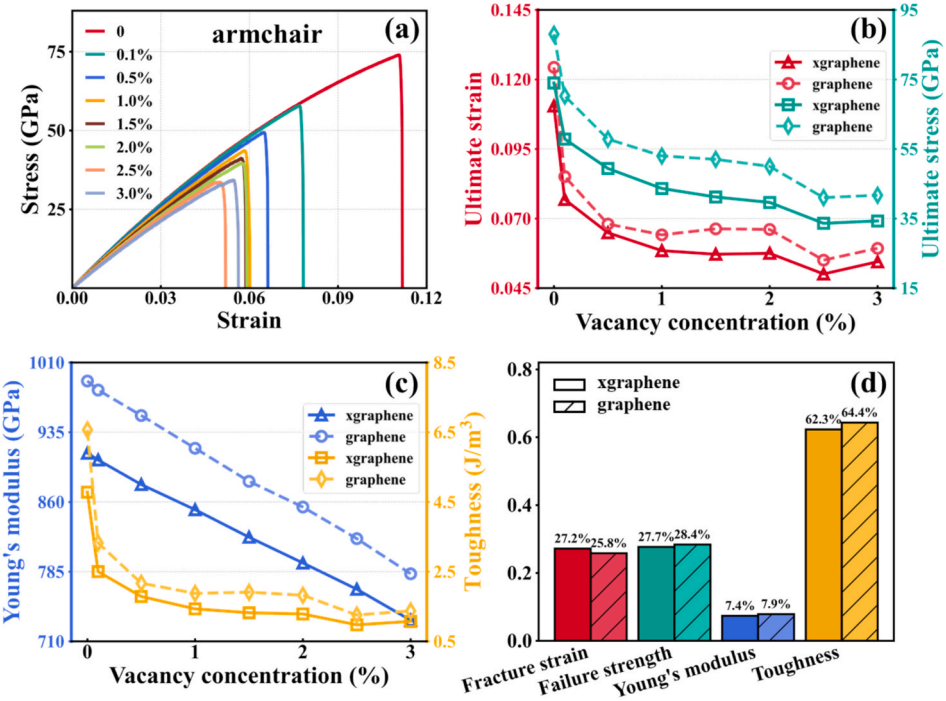

Fig. 9. The vacancy defects effect on xgraphene's mechanical properties along the armchair direction. (a) Stress–strain curves for xgraphene at different vacancy concentrations. (b, c) Variation of ultimate strain, ultimate stress, Young's modulus, and toughness with increasing random vacancy concentrations for xgraphene and graphene. (d) Coefficient of variation for the mechanical properties of xgraphene with varying random vacancy concentrations.

armchair direction, xgraphene's ultimate stress decreases from 73.97 GPa to 31.53 GPa, a 57 % reduction; ultimate strain decreases from 0.110 to 0.039, a 65 % decrease; Young's modulus decreases from 912.5 GPa to 867.8 GPa, a 4.9 % reduction; and toughness decreases from 4.78 J/m^3 to 0.68 J/m^3, an 86 % decrease.

Fig. 10 (a, b) show the von Mises stress distribution of xgraphene during tensile strain with a 3 nm rectangular crack. The results show significant stress concentrations near the crack tip, with faster crack propagation occurring at longer crack lengths. In particular, longer cracks led to more pronounced stress concentrations, accelerating the

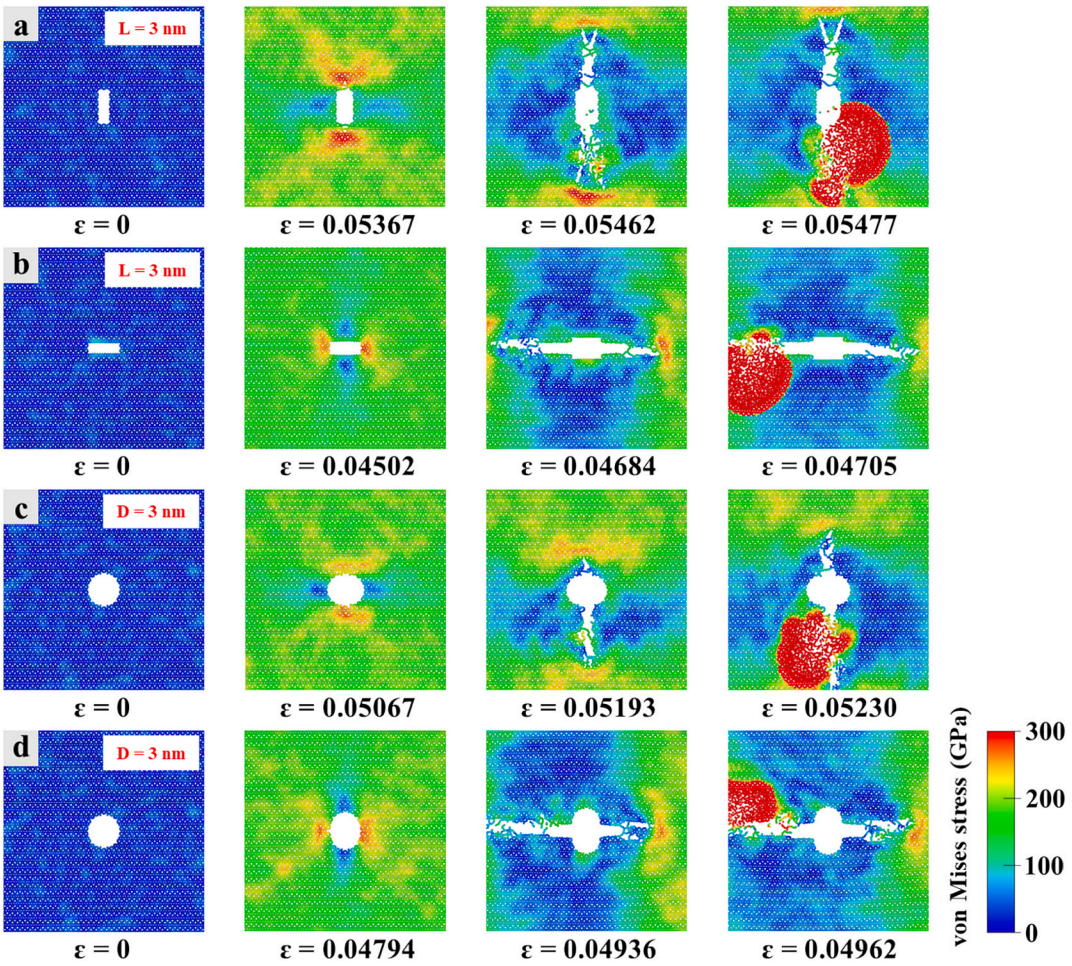

Fig. 10. Von Mises stress distribution in xgraphene with various defects. (a) Von Mises stress for a 3 nm rectangular defect under uniaxial tension along the zigzag direction. (b) Von Mises stress for a 3 nm rectangular defect under uniaxial tension along the armchair direction. (c) Von Mises stress for a 3 nm circular defect under uniaxial tension along the zigzag direction. (d) Von Mises stress for a 3 nm circular defect under uniaxial tension along the armchair direction.

fracture process. This phenomenon is especially significant as crack length increases. Shorter cracks require more strain to propagate. While crack-induced stress concentration is a widely recognized phenomenon in material science, xgraphene exhibits distinctive behavior due to its unique anisotropic properties. Specifically, xgraphene shows a more pronounced sensitivity to crack length along the armchair direction compared to the zigzag direction. This difference underscores the importance of considering directional mechanical properties when studying fracture behaviors in xgraphene, which could significantly influence its use in nanotechnology and engineering applications that require precise material properties.

3.5.2. *Circular void defects*

To further explore the impact of defect geometry, we introduced circular void defects with diameters of 1, 2, 3, and 4 nm at the center of the xgraphene model. Uniaxial tensile simulations were performed in the directions of zigzag and armchair, and the results were compared with the defect-free xgraphene. Fig. 11 (c, d) show the stress–strain curves for xgraphene under tensile strain with circular voids of varying diameters. Larger void diameters led to earlier failure and lower strain-to-break values. As the void diameter increases from 0 to 4 nm, the following changes were observed along the zigzag direction: Ultimate stress decreases from 63.34 GPa to 36.13 GPa, marking a 43 % reduction; ultimate strain decreases from 0.093 to 0.047, a decrease of 50 %; Young's modulus decreases from 903.2 GPa to 854.6 GPa, a 5.4 % reduction; and toughness decreases from 3.39 J/m^3 to 0.96 J/m^3, a 72 % decrease. Along the armchair direction, xgraphene's ultimate stress decreases from 73.97 GPa to 38.82 GPa, a 48 % reduction; ultimate strain decreases from 0.110 to 0.048, a 56 % decrease; Young's modulus decreases from 912.5 GPa to 864.0 GPa, a 5.3 % reduction; and toughness decreases from 4.78 J/m^3 to 1.03 J/m^3, a 78 % decrease. Fig. 10 (c, d) illustrate the von Mises stress distribution of xgraphene with a 3 nm circular void during tensile strain. Similar to rectangular cracks, circular voids induced stress concentrations around their edges, promoting crack initiation at the void boundary. Larger voids cause more extensive and severe stress concentration, significantly impairing the material's strength and toughness. The effect of void diameter on the mechanical properties and fracture mode is more pronounced along the armchair direction, which demonstrates greater sensitivity to changes in void size. These results emphasize the need to account for directional properties when studying the fracture behavior of xgraphene, which is particularly relevant for applications in nanotechnology and advanced engineering fields.

3.5.3. *Radial distribution function analyze*

To further investigate the formation of the amorphous phase observed during tensile fracture, we utilized the RDF, which describes the atomic density distribution. RDFs are useful for analyzing the spatial arrangement of atoms, particularly in materials that exhibit amorphous behavior, which lacks a regular periodic structure. By examining the RDF data, we can assess structural changes that occur as xgraphene undergoes tensile deformation and transitions into an amorphous state.

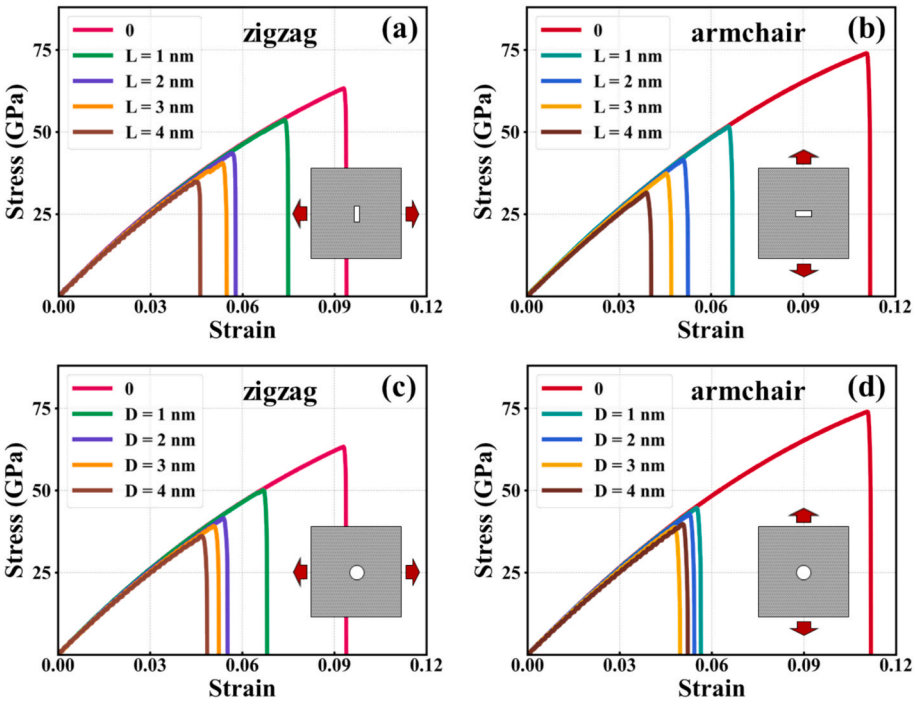

Fig. 11. Mechanical response of xgraphene with different defects. (a) Stress–strain curves for xgraphene with different lengths of rectangular defects under uniaxial tension along the zigzag direction. (b) Stress–strain curves for xgraphene with different lengths of rectangular defects under uniaxial tension along the armchair direction. (c) Stress–strain curves for xgraphene with different diameters of circular defects under uniaxial tension along the zigzag direction. (d) Stress–strain curves for xgraphene with different diameters of circular defects under uniaxial tension along the armchair direction.

We selected samples with 3 nm rectangular cracks and 3 nm circular voids and analyzed their RDFs during tensile strain along both zigzag and armchair directions. The RDF data were collected at several key stages, corresponding to the von Mises stress distribution: the first RDF data reflects the structure after relaxation but before stretching; the second reflects the structure just before fracture initiation; the third reflects the process of crack initiation and growth, followed by nine data showing the development of the amorphous phase. Based on the analysis of Fig. 12 RDF data, we noted that with increasing strain, peak positions on the RDF curves shifted, peak heights decreased, and troughs between peaks filled gradually, indicating a loss of crystalline order. Before fracture, due to stretching, atomic bond lengths are elongated, causing a rightward shift in peak positions; after fracture but before the appearance of the amorphous phase, the peak position remains nearly unchanged; once the amorphous phase appears, atomic bonds start to break, causing peak positions to shift rightwards noticeably and peak heights to decrease. This indicates that xgraphene exhibits an amorphous phase in the later stages of tensile strain.

3.6. Anisotropic mechanical response and comparison with other materials

Xgraphene exhibits anisotropic mechanical properties, which result from its unique structural arrangement. These properties vary along different crystallographic axes. In practical applications, materials often experience stress and strain from multiple directions. Understanding the anisotropic mechanical response of xgraphene is critical for predicting its behavior under complex loading conditions, thereby improving its reliability for engineering applications.

To investigate the anisotropic mechanical response, we conducted uniaxial tension simulations along both the zigzag and armchair directions, using a model consisting of 26,880 atoms at 300 K. The resulting stress–strain curves for xgraphene, compared with those of graphene under similar conditions, are shown in Fig. 13. Along the zigzag direction, the ultimate stress is 63.34 GPa, and 73.97 GPa along the armchair direction, which is 17 % higher in the armchair direction than in the zigzag direction. In comparison, the ultimate stress of graphene is 103.00 GPa along the zigzag direction and 88.00 GPa along the armchair direction, which is 17 % higher in the zigzag direction than in the armchair direction. The ultimate strain of xgraphene is 0.093 along the zigzag direction and 0.110 along the armchair direction, which is 18 % higher than that in the zigzag direction. In contrast, the ultimate strain of graphene is 0.177 along the zigzag direction and 0.124 along the armchair direction, which is 43 % higher in the zigzag direction than in the armchair direction. Xgraphene's Young's modulus is 903.2 GPa along the zigzag direction and 912.5 GPa along the armchair direction, which is 1.0 % higher in the zigzag direction than in the armchair direction. In contrast, the Young's modulus of graphene is 921.7 GPa along the zigzag direction and 990.2 GPa along the armchair direction, which is 7.4 % higher in the armchair direction than in the zigzag direction. In terms of toughness, xgraphene has 3.39 J/m^3 along the zigzag direction and 4.78 J/m^3 along the armchair direction, which is 41 % higher in the armchair direction than in the zigzag direction. In contrast, graphene's toughness is 11.08 J/m^3 along the zigzag direction and 6.57 J/m^3 along the armchair direction, 69 % higher in the zigzag direction than in the armchair direction. The anisotropy of xgraphene is not significant compared to graphene, and the strength of the armchair direction is significantly higher than that of the zigzag direction.

The mechanical properties of xgraphene are different from those of graphene in different directions, which is likely due to its unique carbon atom arrangement structure, which is different from the regular hexagonal structure of graphene. Wang et al. also demonstrated anisotropy in xgraphene's electrical properties [34]. Xgraphene's anisotropic mechanical and electrical properties expand its potential applications.

The mechanical properties of xgraphene at 1 K, as calculated in Section 3.3 of this study, generally agree well with the results calculated by Wang et al. using density functional theory (DFT). At 1 K, the ultimate stress of xgraphene in the zigzag direction is 90.81 GPa, while in the armchair direction, it is 91.16 GPa. In contrast, the DFT calculations by Wang et al. report ultimate stresses of 99.53 GPa in the zigzag

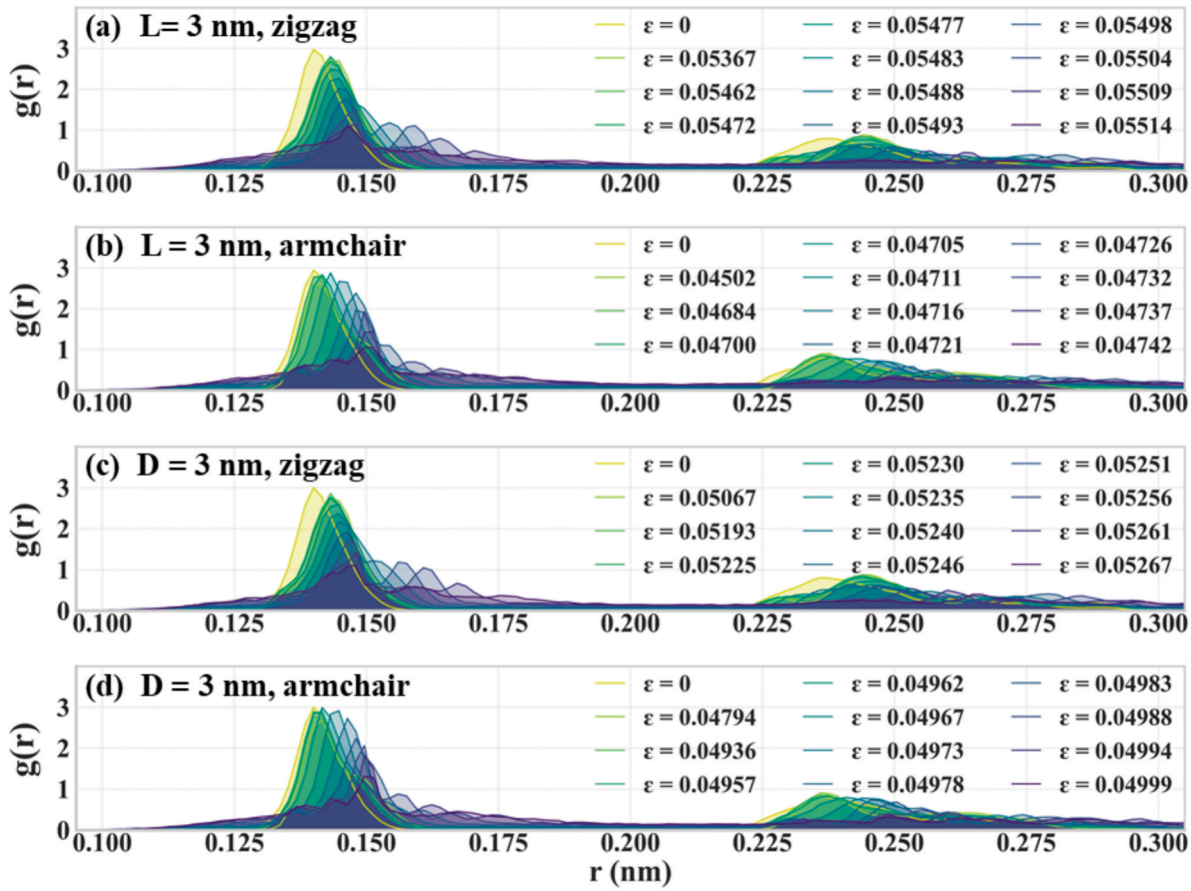

Fig. 12. RDF analysis for xgraphene with different defects and directions. (a) RDF for xgraphene with a 3 nm rectangular crack defect under uniaxial tension along the zigzag direction. (b) RDF for xgraphene with a 3 nm rectangular crack defect under uniaxial tension along the armchair direction. (c) RDF for xgraphene with a 3 nm circular void defect under uniaxial tension along the zigzag direction. (d) RDF for xgraphene with a 3 nm circular void defect under uniaxial tension along the armchair direction.

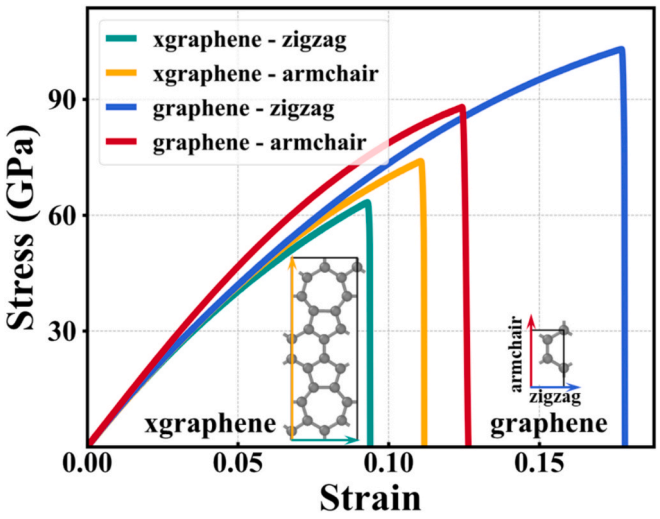

Fig. 13. Stress–strain curves of xgraphene and graphene under uniaxial tension along zigzag and armchair directions at 300 K.

direction and 104.9 GPa in the armchair direction. Our results differ from theirs by 8.8 % in the zigzag direction and 13 % in the armchair direction. For ultimate strain, the values for xgraphene at 1 K are 0.192 in the zigzag direction and 0.174 in the armchair direction. Wang et al. calculated ultimate strains of 0.190 in the zigzag direction and 0.220 in the armchair direction. The differences between our results and theirs are 1.0 % in the zigzag direction and 21 % in the armchair direction. Regarding Young's modulus, our calculations show values of 912.4 GPa for the zigzag direction and 930.8 GPa for the armchair direction. Wang et al. found Young's moduli of 896.1 GPa and 940.5 GPa for the zigzag and armchair directions, respectively. The discrepancies between our results and theirs are 1.8 % in the zigzag direction and 1.0 % in the armchair direction. Overall, the mechanical properties of xgraphene at 1 K, as calculated in this study, exhibit excellent consistency with the previous DFT results.

Additionally, we compared the mechanical properties of xgraphene with those of other 2D carbon allotropes. Fig. 14 presents a comparison of the Young's modulus, ultimate strain, and ultimate stress of xgraphene and other materials at 300 K, obtained from MD simulations. Although the Young's modulus of xgraphene is lower than that of graphene, it surpasses that of γ-graphyne [71], phagraphene [72], popgraphene [73], and ψ-graphene [74] in both the zigzag and armchair directions. The ultimate strain of xgraphene is relatively low compared to other materials. However, in the zigzag direction, it is close to that of popgraphene [73], while in the armchair direction, it is comparable to γ-graphyne [71]. As for ultimate stress, xgraphene exhibits lower values compared to the other materials. However, in the zigzag direction, its ultimate stress is similar to that of γ-graphyne [71], while in the armchair direction, it is closer to phagraphene [72], and it remains significantly higher than γ-graphyne [71]. The high tensile strength and Young's modulus of xgraphene suggest its potential for practical applications.

Xgraphene shows promising mechanical properties, with a higher

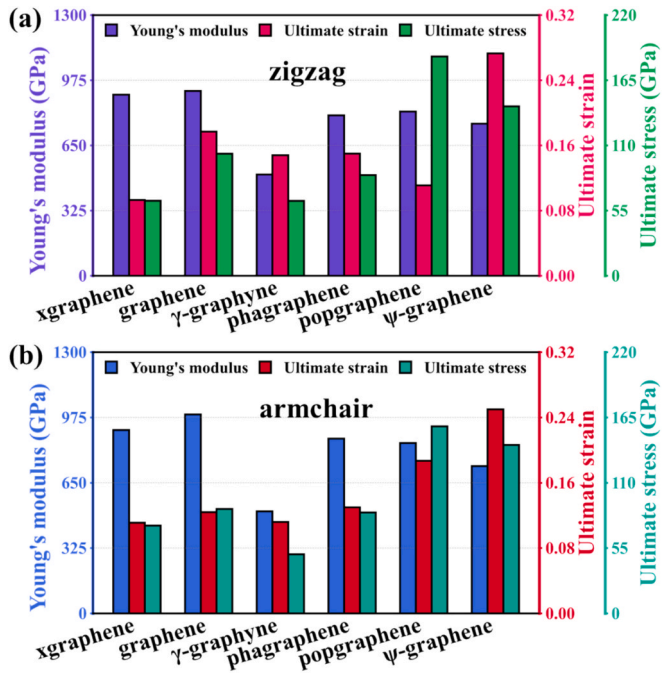

Fig. 14. Comparison of the Young's modulus, ultimate strain, and ultimate stress of xgraphene and other 2D materials at 300 K. (a) Data for the zigzag direction. (b) Data for the armchair direction.

Young's modulus than several other 2D carbon allotropes and comparable ultimate strain and stress values. Its performance in different crystallographic directions suggests it could be a competitive material for specific engineering applications, particularly in directions where other materials may not perform as well [75–79].

4. Conclusions

This study extensively investigated the mechanical properties of xgraphene through MD simulations, analyzing its responses and behaviors under various conditions, including size, strain rate, temperature, vacancy defects, rectangular crack defects, and circular void defects. Our MD results suggest that strain rate influences simulation results, with mechanical properties stabilizing as strain rates fall below 1×10^9/s. The mechanical properties of xgraphene differ significantly between stretching along zigzag and armchair directions, with Young's moduli of 903.2 GPa and 912.5 GPa at 300 K, respectively, the latter exhibiting higher stiffness. Temperature has a pronounced effect on xgraphene's mechanical properties. As the temperature increases, the material's mechanical performance decreases. This behavior is closely related to changes in atomic energy and movement. For instance, increasing temperature from 1 K to 900 K reduces Young's modulus along zigzag direction from 912.4 GPa to 854.4 GPa, a decrease of 6.4 % with a coefficient of variation of 2.4 %, and along armchair direction from 930.8 GPa to 871.2 GPa, a decrease of 6.4 % with a coefficient of variation of 2.3 %. The introduction of vacancy defects significantly impacts xgraphene's mechanical properties, leading to localized strain concentrations around defects and altering the material's overall elastic performance. Increasing vacancy defect concentration from 0 to 3 % reduces Young's modulus along zigzag direction from 903.2 GPa to 702.6 GPa, a 22 % reduction with a coefficient of variation of 8.5 %, and along armchair direction from 912.5 GPa to 732.8 GPa, a 20 % reduction with a coefficient of variation of 7.4 %. Different sizes and shapes of defects also have a significant impact on xgraphene's mechanical properties. For rectangular crack defects, increasing length from 0 to 4 nm decreases Young's modulus along zigzag direction from 903.2 GPa to 859.2 GPa, a 4.9 % reduction, with a coefficient of variation of 1.8 %; and along armchair direction from 912.5 GPa to 867.8 GPa, a 4.9 % reduction, with a coefficient of variation of 1.8 %. Similarly, for circular void defects, increasing diameter from 0 to 4 nm decreases Young's modulus along zigzag direction from 903.2 GPa to 854.6 GPa, a 5.4 % reduction, with a coefficient of variation of 2.1 %; and along armchair direction from 912.5 GPa to 864.0 GPa, a 5.3 % reduction, with a coefficient of variation of 2.0 %. Through analysis of von Mises stress, we identified stress concentrations at defect edges, which promote defect propagation and thereby significantly affect material mechanical performance. Furthermore, analysis of RDF data revealed the occurrence of amorphous phases during uniaxial tension of xgraphene.

In summary, this study systematically investigated the mechanical properties of xgraphene through MD simulations, revealing its mechanical response characteristics and fracture behavior mechanisms under different conditions. These findings are crucial not only for understanding the mechanical nature of two-dimensional materials but also for providing theoretical support and experimental guidance for their widespread applications in nanotechnology and materials engineering. Future research will continue to explore novel material design and optimization pathways, advancing the application and development of two-dimensional materials in advanced technological fields.

Funding

This research was funded by the Shenzhen Science and Technology Program (Grant No. KQTD20200820113045081), the National Natural Science Foundation of China (grant No. 12272378), the Strategic Priority Research Program of the Chinese Academy of Sciences (grant No. XDB0620103), Educational Commission of Hubei Province of China (Grant No. Q20233005), Doctoral Research Initiation Fund of Hubei University of Technology (grant No. XJ2024008301), and the High-level Innovation Research Institute Program of Guangdong Province (grant No. 2020B0909010003).

CRediT authorship contribution statement

Qing Peng: Writing – review & editing, Supervision, Funding acquisition, Formal analysis, Conceptualization. **Ao Li:** Writing – original draft, Data curation. **Gen Chen:** Software, Methodology. **Zeyu Huang:** Software, Methodology. **Xue Chen:** Writing – review & editing. **Xintian Cai:** Software, Methodology. **Zhongwei Hu:** Writing – review & editing, Funding acquisition. **Xiao-Jia Chen:** Writing – review & editing.

Declaration of competing interest

The authors declare that they have no known competing financial interests or personal relationships that could have appeared to influence the work reported in this paper.

Data availability

No data was used for the research described in the article.

References

[1] K.S. Novoselov, A.K. Geim, S.V. Morozov, D. Jiang, Y. Zhang, S.V. Dubonos, I. V. Grigorieva, A.A. Firsov, Electric field effect in atomically thin carbon films, Retrieved from, *Science* 306 (5696) (2004) 666–669, https://www.ncbi.nlm.nih.gov/pubmed/15499015, https://doi.org/10.1126/science.1102896.

[2] K.S. Novoselov, A.K. Geim, S.V. Morozov, D. Jiang, M.I. Katsnelson, I. V. Grigorieva, S.V. Dubonos, A.A. Firsov, Two-dimensional gas of massless dirac fermions in graphene, Retrieved from, *Nature* 438 (7065) (2005) 197–200, https://www.ncbi.nlm.nih.gov/pubmed/16281030, https://doi.org/10.1038/nature04233.

[3] Y. Zhang, Y.W. Tan, H.L. Stormer, P. Kim, Experimental observation of the quantum hall effect and berry's phase in graphene, Retrieved from, *Nature* 438 (7065) (2005) 201–204, https://www.ncbi.nlm.nih.gov/pubmed/16281031, https://doi.org/10.1038/nature04235.

[4] C. Lee, X. Wei, J.W. Kysar, J. Hone, Measurement of the elastic properties and intrinsic strength of monolayer graphene, Retrieved from, *Science* 321 (5887)

(2008) 385–388, https://www.ncbi.nlm.nih.gov/pubmed/18635798, https://doi.org/10.1126/science.1157996.
[5] P. Zhang, L. Ma, F. Fan, Z. Zeng, C. Peng, P.E. Loya, Z. Liu, Y. Gong, J. Zhang, X. Zhang, P.M. Ajayan, T. Zhu, J. Lou, Fracture toughness of graphene, Retrieved from, *Nat Commun* 5 (2014) 3782, https://www.ncbi.nlm.nih.gov/pubmed/24777167, https://doi.org/10.1038/ncomms4782.
[6] F. Liu, P. Ming, J. Li, Ab initiocalculation of ideal strength and phonon instability of graphene under tension, *Phys. Rev. B* 76 (6) (2007), https://doi.org/10.1103/PhysRevB.76.064120. Retrieved from <Go to ISI>://WOS:000249155200035.
[7] B. Deng, J. Hou, H. Zhu, S. Liu, E. Liu, Y. Shi, Q. Peng, The normal-auxeticity mechanical phase transition in graphene, *2D Mater.* 4 (2) (2017), https://doi.org/10.1088/2053-1583/aa61e5. Retrieved from <Go to ISI>://WOS:000397619900001.
[8] G. Eda, G. Fanchini, M. Chhowalla, Large-area ultrathin films of reduced graphene oxide as a transparent and flexible electronic material, Retrieved from, *Nat Nanotechnol* 3 (5) (2008) 270–274, https://www.ncbi.nlm.nih.gov/pubmed/18654522, https://doi.org/10.1038/nnano.2008.83.
[9] K.S. Kim, Y. Zhao, H. Jang, S.Y. Lee, J.M. Kim, K.S. Kim, J.H. Ahn, P. Kim, J. Y. Choi, B.H. Hong, Large-scale pattern growth of graphene films for stretchable transparent electrodes, Retrieved from, *Nature* 457 (7230) (2009) 706–710, https://www.ncbi.nlm.nih.gov/pubmed/19145232, https://doi.org/10.1038/nature07719.
[10] F. Xia, D.B. Farmer, Y.M. Lin, P. Avouris, Graphene field-effect transistors with high on/off current ratio and large transport band gap at room temperature, Retrieved from, *Nano Lett* 10 (2) (2010) 715–718, https://www.ncbi.nlm.nih.gov/pubmed/20092332, https://doi.org/10.1021/nl9039636.
[11] S.C. O'hern, C.A. Stewart, M.S. Boutilier, J.C. Idrobo, S. Bhaviripudi, S.K. Das, J. Kong, T. Laoui, M. Atieh, & R. Karnik. (2012). Selective molecular transport through intrinsic defects in a single layer of cvd graphene. *Acs Nano, 6*(11), 10130-10138. Retrieved from https://www.ncbi.nlm.nih.gov/pubmed/23030691. doi: 10.1021/nn303869m.
[12] S.C. O'hern, M.S. Boutilier, J.C. Idrobo, Y. Song, J. Kong, T. Laoui, M. Atieh, & R. Karnik. (2014). Selective ionic transport through tunable subnanometer pores in single-layer graphene membranes. *Nano Lett, 14*(3), 1234-1241. Retrieved from https://www.ncbi.nlm.nih.gov/pubmed/24490698. doi:10.1021/nl404118f.
[13] S.P. Koenig, L. Wang, J. Pellegrino, J.S. Bunch, Selective molecular sieving through porous graphene, Retrieved from, *Nat Nanotechnol* 7 (11) (2012) 728–732, https://www.ncbi.nlm.nih.gov/pubmed/23042491, https://doi.org/10.1038/nnano.2012.162.
[14] J.S. Bunch, A.M. Van Der Zande, S.S. Verbridge, I.W. Frank, D.M. Tanenbaum, J. M. Parpia, H.G. Craighead, P.L. Mceuen, Electromechanical resonators from graphene sheets, Retrieved from, *Science* 315 (5811) (2007) 490–493, https://www.ncbi.nlm.nih.gov/pubmed/17255506, https://doi.org/10.1126/science.1136836.
[15] Y. Yang, X. Yang, L. Liang, Y. Gao, H. Cheng, X. Li, M. Zou, R. Ma, Q. Yuan, X. Duan, Large-area graphene-nanomesh/carbon-nanotube hybrid membranes for ionic and molecular nanofiltration, Retrieved from, *Science* 364 (6445) (2019) 1057–1062, https://www.ncbi.nlm.nih.gov/pubmed/31197007, https://doi.org/10.1126/science.aau5321.
[16] K.S. Kumar, H. Van Swygenhoven, S. Suresh, Mechanical behavior of nanocrystalline metals and alloys11the golden jubilee issue—selected topics in materials science and engineering: Past, present and future, edited by s, Suresh. *Acta Materialia* 51 (19) (2003) 5743–5774, https://doi.org/10.1016/j.actamat.2003.08.032. Retrieved from <Go to ISI>://WOS:000186603200005.
[17] D.E. Jiang, V.R. Cooper, S. Dai, Porous graphene as the ultimate membrane for gas separation, Retrieved from, *Nano Lett* 9 (12) (2009) 4019–4024, https://www.ncbi.nlm.nih.gov/pubmed/19995080, https://doi.org/10.1021/nl9021946.
[18] J. Bai, X. Zhong, S. Jiang, Y. Huang, X. Duan, Graphene nanomesh, Retrieved from, *Nat Nanotechnol* 5 (3) (2010) 190–194, https://www.ncbi.nlm.nih.gov/pubmed/20154685, https://doi.org/10.1038/nnano.2010.8.
[19] J. Tong, Y. Fu, D. Domaretskiy, F. Della Pia, P. Dagar, L. Powell, D. Bahamon, S. Huang, B. Xin, R.N. Costa Filho, L.F. Vega, I.V. Grigorieva, F.M. Peeters, A. Michaelides, M. Lozada-Hidalgo, Control of proton transport and hydrogenation in double-gated graphene, *Nature* 630 (8017) (2024) 619–624, https://doi.org/10.1038/s41586-024-07435-8.
[20] Q. Peng, C. Liang, W. Ji, S. De, A theoretical analysis of the effect of the hydrogenation of graphene to graphane on its mechanical properties, Retrieved from, *Phys Chem Chem Phys* 15 (6) (2013) 2003–2011, https://www.ncbi.nlm.nih.gov/pubmed/23257777, https://doi.org/10.1039/c2cp43360e.
[21] Q. Peng, A.K. Dearden, X.J. Chen, C. Huang, X. Wen, S. De, Peculiar pressure effect on poisson ratio of graphone as a strain damper, Retrieved from, *Nanoscale* 7 (22) (2015) 9975–9979, https://www.ncbi.nlm.nih.gov/pubmed/25853996, https://doi.org/10.1039/c4nr07665f.
[22] Q. Cao, X. Geng, H. Wang, P. Wang, A. Liu, Y. Lan, Q. Peng, A review of current development of graphene mechanics, *Crystals* 8 (9) (2018), https://doi.org/10.3390/cryst8090357. Retrieved from <Go to ISI>://WOS:000447917200026.
[23] Y. Liu, X. Chen, Mechanical properties of nanoporous graphene membrane, *J. Appl. Phys.* 115 (3) (2014), https://doi.org/10.1063/1.4862312. Retrieved from <Go to ISI>://WOS:000330615500063.
[24] D. Cohen-Tanugi, J.C. Grossman, Water desalination across nanoporous graphene, Retrieved from, *Nano Lett* 12 (7) (2012) 3602–3608, https://www.ncbi.nlm.nih.gov/pubmed/22668008, https://doi.org/10.1021/nl3012853.
[25] D. Cohen-Tanugi, J.C. Grossman, Mechanical strength of nanoporous graphene as a desalination membrane, Retrieved from, *Nano Lett* 14 (11) (2014) 6171–6178, https://www.ncbi.nlm.nih.gov/pubmed/25357231, https://doi.org/10.1021/nl502399y.
[26] S. Garaj, S. Liu, J.A. Golovchenko, D. Branton, Molecule-hugging graphene nanopores, Retrieved from, *Proc Natl Acad Sci U S A* 110 (30) (2013) 12192–12196, https://www.ncbi.nlm.nih.gov/pubmed/23836648, https://doi.org/10.1073/pnas.1220012110.
[27] G.F. Schneider, S.W. Kowalczyk, V.E. Calado, G. Pandraud, H.W. Zandbergen, L. M. Vandersypen, C. Dekker, DNA translocation through graphene nanopores, Retrieved from, *Nano Lett* 10 (8) (2010) 3163–3167, https://www.ncbi.nlm.nih.gov/pubmed/20608744, https://doi.org/10.1021/nl102069z.
[28] C.A. Merchant, K. Healy, M. Wanunu, V. Ray, N. Peterman, J. Bartel, M. D. Fischbein, K. Venta, Z. Luo, A.T. Johnson, M. Drndic, DNA translocation through graphene nanopores, Retrieved from, *Nano Lett* 10 (8) (2010) 2915–2921, https://www.ncbi.nlm.nih.gov/pubmed/20698604, https://doi.org/10.1021/nl101046t.
[29] Q. Zheng, Y. Geng, S. Wang, Z. Li, J.-K. Kim, Effects of functional groups on the mechanical and wrinkling properties of graphene sheets, *Carbon* 48 (15) (2010) 4315–4322, https://doi.org/10.1016/j.carbon.2010.07.044.
[30] J.-S. Gao, S.-C. Shiu, J.-L. Tsai, Retrieved from, Mechanical Properties of Polymer near Graphite Sheet. 47 (4) (2013) 449–458, https://journals.sagepub.com/doi/abs/10.1177/0021998312441040, https://doi.org/10.1177/0021998312441040.
[31] C.M. Hadden, D.R. Klimek-Mcdonald, E.J. Pineda, J.A. King, A.M. Reichanadter, I. Miskioglu, S. Gowtham, G.M. Odegard, Mechanical properties of graphene nanoplatelet/carbon fiber/epoxy hybrid composites: Multiscale modeling and experiments, Retrieved from, *Carbon* 95 (2015) 100–112, https://www.sciencedirect.com/science/article/pii/S0008622315301457, https://doi.org/10.1016/j.carbon.2015.08.026.
[32] Y. Yang, X. Xu, Mechanical properties of graphyne and its family – a molecular dynamics investigation, Retrieved from, *Comput. Mater. Sci* 61 (2012) 83–88, https://www.sciencedirect.com/science/article/pii/S0927025612001991, https://doi.org/10.1016/j.commatsci.2012.03.052.
[33] Q. Peng, Z. Chen, S.J.M.o.A.M. De, & Structures. (2015). A density functional theory study of the mechanical properties of graphane with van der waals corrections. *22*(9), 717-721.
[34] S. Wang, Y. Si, B. Yang, E. Ruckenstein, H. Chen, Two-dimensional carbon-based auxetic materials for broad-spectrum metal-ion battery anodes, Retrieved from, *J Phys Chem Lett* 10 (12) (2019) 3269–3275, https://www.ncbi.nlm.nih.gov/pubmed/31141368, https://doi.org/10.1021/acs.jpclett.9b00905.
[35] S. Plimpton. (1995). Fast parallel algorithms for short-range molecular dynamics. *Journal of Computational Physics, 117*(1), 1-19. Retrieved from <Go to ISI>://WOS:A1995QK44800001. doi:10.1006/jcph.1995.1039.
[36] A. Stukowski, Visualization and analysis of atomistic simulation data with ovito–the open visualization tool, in: *Modelling and Simulation in Materials Science and Engineering, 18*(1). Retrieved from <go to ISI>://WOS:000272791800012, 2010, https://doi.org/10.1088/0965-0393/18/1/015012.
[37] T.C. O'connor, J. Andzelm, & M.O.J.T.J.o.c.p. Robbins. (2015). Airebo-m: A reactive model for hydrocarbons at extreme pressures. *142*(2).
[38] H. Zhao, K. Min, N.R. Aluru, Size and chirality dependent elastic properties of graphene nanoribbons under uniaxial tension, Retrieved from, *Nano Lett* 9 (8) (2009) 3012–3015, https://www.ncbi.nlm.nih.gov/pubmed/19719113, https://doi.org/10.1021/nl901448z.
[39] T. Zhang, X. Li, S. Kadkhodaei, H. Gao, Flaw insensitive fracture in nanocrystalline graphene, Retrieved from, *Nano Lett* 12 (9) (2012) 4605–4610, https://www.ncbi.nlm.nih.gov/pubmed/22889375, https://doi.org/10.1021/nl301908b.
[40] Y. Wei, J. Wu, H. Yin, X. Shi, R. Yang, M. Dresselhaus, The nature of strength enhancement and weakening by pentagon-heptagon defects in graphene, Retrieved from, *Nat Mater* 11 (9) (2012) 759–763, https://www.ncbi.nlm.nih.gov/pubmed/22751178, https://doi.org/10.1038/nmat3370.
[41] O.A. Shenderova, D.W. Brenner, A. Omeltchenko, X. Su, L.H. Yang, Atomistic modeling of the fracture of polycrystalline diamond, *Phys. Rev. B* 61 (6) (2000) 3877–3888, https://doi.org/10.1103/PhysRevB.61.3877. Retrieved from <Go to ISI>://WOS:000085364700026.
[42] R. Grantab, V.B. Shenoy, R.S. Ruoff, Anomalous strength characteristics of tilt grain boundaries in graphene, Retrieved from, *Science* 330 (6006) (2010) 946–948, https://www.ncbi.nlm.nih.gov/pubmed/21071664, https://doi.org/10.1126/science.1196893.
[43] H. Zhao, N.R. Aluru, Temperature and strain-rate dependent fracture strength of graphene, *J. Appl. Phys.* 108 (6) (2010), https://doi.org/10.1063/1.3488620. Retrieved from <Go to ISI>://WOS:000282646400144.
[44] Z. Qi, F. Zhao, X. Zhou, Z. Sun, H.S. Park, H. Wu, A molecular simulation analysis of producing monatomic carbon chains by stretching ultranarrow graphene nanoribbons, Retrieved from, *Nanotechnology* 21 (26) (2010) 265702, https://www.ncbi.nlm.nih.gov/pubmed/20522927, https://doi.org/10.1088/0957-4484/21/26/265702.
[45] Y.I. Jhon, S.-E. Zhu, J.-H. Ahn, M.S. Jhon, The mechanical responses of tilted and non-tilted grain boundaries in graphene, *Carbon* 50 (10) (2012) 3708–3716, https://doi.org/10.1016/j.carbon.2012.03.044. Retrieved from <Go to ISI>://WOS:000305851700040.
[46] J.-W. Jiang, J.-S. Wang, B. Li, Young's modulus of graphene: A molecular dynamics study, Retrieved from, *Phys. Rev. B* 80 (11) (2009) 113405, https://link.aps.org/doi/10.1103/PhysRevB.80.113405, https://doi.org/10.1103/PhysRevB.80.113405.
[47] M.A.N. Dewapriya, A. Srikantha Phani, R.K.N.D. Rajapakse, Influence of temperature and free edges on the mechanical properties of graphene, in: *Modelling and Simulation in Materials Science and Engineering, 21*(6). Retrieved from <go to ISI>://WOS:000323290600018, 2013, https://doi.org/10.1088/0965-0393/21/6/065017.

[48] A.W. Tsen, L. Brown, M.P. Levendorf, F. Ghahari, P.Y. Huang, R.W. Havener, C. S. Ruiz-Vargas, D.A. Muller, P. Kim, Retrieved from, J. Park. Tailoring Electrical Transport across Grain Boundaries in Polycrystalline Graphene. Science 336 (6085) (2012) 1143–1146, https://www.ncbi.nlm.nih.gov/pubmed/22654054, https://doi.org/10.1126/science.1218948.
[49] O.V. Yazyev, S.G. Louie, Electronic transport in polycrystalline graphene, Retrieved from, *Nat Mater* 9 (10) (2010) 806–809, https://www.ncbi.nlm.nih.gov/pubmed/20729847, https://doi.org/10.1038/nmat2830.
[50] Z. Zhang, Y. Yang, F. Xu, L. Wang, B.I. Yakobson, Unraveling the sinuous grain boundaries in graphene, *Adv. Funct. Mater.* 25 (3) (2014) 367–373, https://doi.org/10.1002/adfm.201403024. Retrieved from <Go to ISI>://WOS:000347897000003.
[51] J. Zhang, J. Zhao, J. Lu, Intrinsic strength and failure behaviors of graphene grain boundaries, Retrieved from, *ACS Nano* 6 (3) (2012) 2704–2711, https://www.ncbi.nlm.nih.gov/pubmed/22369492, https://doi.org/10.1021/nn3001356.
[52] A. Bagri, S.P. Kim, R.S. Ruoff, V.B. Shenoy, Thermal transport across twin grain boundaries in polycrystalline graphene from nonequilibrium molecular dynamics simulations, Retrieved from, *Nano Lett* 11 (9) (2011) 3917–3921, https://www.ncbi.nlm.nih.gov/pubmed/21863804, https://doi.org/10.1021/nl202118d.
[53] H. Zhang, G. Lee, K. Cho, Thermal transport in graphene and effects of vacancy defects, *Phys. Rev. B* 84 (11) (2011), https://doi.org/10.1103/PhysRevB.84.115460. Retrieved from <Go to ISI>://WOS:000295263600014.
[54] O.V. Yazyev, L. Helm, Defect-induced magnetism in graphene, *Phys. Rev. B* 75 (12) (2007), https://doi.org/10.1103/PhysRevB.75.125408. Retrieved from <Go to ISI>://WOS:000245330200085.
[55] J.J. Palacios, J. Fernández-Rossier, L. Brey, Vacancy-induced magnetism in graphene and graphene ribbons, *Phys. Rev. B* 77 (19) (2008), https://doi.org/10.1103/PhysRevB.77.195428. Retrieved from <Go to ISI>://WOS:000256971600136.
[56] M.H. Gass, U. Bangert, A.L. Bleloch, P. Wang, R.R. Nair, A.K. Geim, Free-standing graphene at atomic resolution, Retrieved from, *Nat Nanotechnol* 3 (11) (2008) 676–681, https://www.ncbi.nlm.nih.gov/pubmed/18989334, https://doi.org/10.1038/nnano.2008.280.
[57] A. Hashimoto, K. Suenaga, A. Gloter, K. Urita, S. Iijima, Direct evidence for atomic defects in graphene layers, Retrieved from, *Nature* 430 (7002) (2004) 870–873, https://www.ncbi.nlm.nih.gov/pubmed/15318216, https://doi.org/10.1038/nature02817.
[58] M.D. Fischbein, M. Drndić, Electron beam nanosculpting of suspended graphene sheets, *Appl. Phys. Lett.* 93 (11) (2008), https://doi.org/10.1063/1.2980518. Retrieved from <Go to ISI>://WOS:000259797900069.
[59] L. Xu, N. Wei, Y. Zheng, Mechanical properties of highly defective graphene: From brittle rupture to ductile fracture, Retrieved from, *Nanotechnology* 24 (50) (2013) 505703, https://www.ncbi.nlm.nih.gov/pubmed/24270887, https://doi.org/10.1088/0957-4484/24/50/505703.
[60] L. Xu, N. Wei, X. Xu, Z. Fan, Y. Zheng, Defect-activated self-assembly of multilayered graphene paper: A mechanically robust architecture with high strength, *J. Mater. Chem. A* 1 (6) (2013) 2002–2010, https://doi.org/10.1039/c2ta00176d. Retrieved from <Go to ISI>://WOS:000314642700011.
[61] J.R. Xiao, J. Staniszewski, J.W. Gillespie, Tensile behaviors of graphene sheets and carbon nanotubes with multiple stone–wales defects, *Mater. Sci. Eng. A* 527 (3) (2010) 715–723, https://doi.org/10.1016/j.msea.2009.10.052. Retrieved from <Go to ISI>://WOS:000273983800042.
[62] J.R. Xiao, J. Staniszewski, J.W. Gillespie, Fracture and progressive failure of defective graphene sheets and carbon nanotubes, *Compos. Struct.* 88 (4) (2009) 602–609, https://doi.org/10.1016/j.compstruct.2008.06.008. Retrieved from <Go to ISI>://WOS:000264252400011.
[63] M.C. Wang, C. Yan, L. Ma, N. Hu, M.W. Chen, Effect of defects on fracture strength of graphene sheets, *Comput. Mater. Sci* 54 (2012) 236–239, https://doi.org/10.1016/j.commatsci.2011.10.032. Retrieved from <Go to ISI>://WOS:000300471500037.
[64] K.I. Tserpes. (2011). Strength of graphenes containing randomly dispersed vacancies. *Acta Mechanica, 223*(4), 669-678. Retrieved from <Go to ISI>://WOS:000302239500001. doi:10.1007/s00707-011-0594-8.
[65] T.-H. Liu, C.-W. Pao, & C.-C. Chang. (2012). Effects of dislocation densities and distributions on graphene grain boundary failure strengths from atomistic simulations. *Carbon, 50*(10), 3465-3472. Retrieved from <Go to ISI>://WOS:000305851700012. doi:10.1016/j.carbon.2012.03.012.
[66] C. Carpenter, D. Maroudas, A. Ramasubramaniam, Mechanical properties of irradiated single-layer graphene, *Appl. Phys. Lett.* 103 (1) (2013), https://doi.org/10.1063/1.4813010. Retrieved from <Go to ISI>://WOS:000321497200029.
[67] R. Ansari, B. Motevalli, A. Montazeri, S. Ajori, Fracture analysis of monolayer graphene sheets with double vacancy defects via md simulation, *Solid State Commun.* 151 (17) (2011) 1141–1146, https://doi.org/10.1016/j.ssc.2011.05.021. Retrieved from <Go to ISI>://WOS:000293940400009.
[68] M.A.N. Dewapriya, R.K.N.D. Rajapakse, Molecular dynamics simulations and continuum modeling of temperature and strain rate dependent fracture strength of graphene with vacancy defects, *J. Appl. Mech.* 81 (8) (2014), https://doi.org/10.1115/1.4027681. Retrieved from <Go to ISI>://WOS:000338203600010.
[69] F. Hao, D. Fang, & Z. Xu. (2011). Mechanical and thermal transport properties of graphene with defects. *Applied Physics Letters, 99*(4). Retrieved from https://doi.org/10.1063/1.3615290. doi:10.1063/1.3615290.
[70] N. Jing, Q. Xue, C. Ling, M. Shan, T. Zhang, X. Zhou, Z. Jiao, Effect of defects on young's modulus of graphene sheets: A molecular dynamics simulation, *RSC Adv.* 2 (24) (2012) 9124–9129, https://doi.org/10.1039/C2RA21228E.
[71] Y. Zhang, Q. Pei, C.J.A.P.L. Wang, Mechanical Properties of Graphynes under Tension: A Molecular Dynamics Study. 101 (8) (2012).
[72] L.F.C. Pereira, B. Mortazavi, M. Makaremi, & T.J.R.a. Rabczuk. (2016). Anisotropic thermal conductivity and mechanical properties of phagraphene: A molecular dynamics study. *6*(63), 57773-57779.
[73] M.L. Pereira Junior, L.A. Ribeiro Junior, W.H. Brandão, A.L. Aguiar, D.S. Galvão, J. M.J.C. De Sousa, Temperature Effects on the Fracture Dynamics and Elastic Properties of Popgraphene Membranes. 21 (17) (2020) 1918–1924.
[74] A. Farzin, M. Etemadi, S. Mehran, S.J.M.T.C. Rouhi, Investigating the Mechanical Properties of Perfect and Defective ψ-Graphene: A Molecular Dynamics Simulation, 37, 2023.
[75] Y. Liu, A. Dobrinsky, B.I. Yakobson, Graphene edge from armchair to zigzag: The origins of nanotube chirality?, Retrieved from, PhysRevLett 105 (23) (2010) 235502, https://www.ncbi.nlm.nih.gov/pubmed/21231478, https://doi.org/10.1103/PhysRevLett.105.235502.
[76] K. Kim, V.I. Artyukhov, W. Regan, Y. Liu, M.F. Crommie, B.I. Yakobson, A. Zettl, Ripping graphene: Preferred directions, Retrieved from, *Nano Lett* 12 (1) (2012) 293–297, https://www.ncbi.nlm.nih.gov/pubmed/22149252, https://doi.org/10.1021/nl203547z.
[77] Y.I. Jhon, Y.M. Jhon, G.Y. Yeom, & M.S. Jhon. (2014). Orientation dependence of the fracture behavior of graphene. *Carbon, 66*, 619-628. Retrieved from <Go to ISI>://WOS:000327575200069. doi:10.1016/j.carbon.2013.09.051.
[78] J. Hou, B. Deng, H. Zhu, Y. Lan, Y. Shi, S. De, L. Liu, P. Chakraborty, F. Gao, Q. Peng, Magic auxeticity angle of graphene, *Carbon* 149 (2019) 350–354, https://doi.org/10.1016/j.carbon.2019.04.057. Retrieved from <Go to ISI>://WOS:000471602000038.
[79] Z. Ni, H. Bu, M. Zou, H. Yi, K. Bi, Y. Chen, Anisotropic mechanical properties of graphene sheets from molecular dynamics, Retrieved from, *Phys. B Condens. Matter* 405 (5) (2010) 1301–1306, https://www.sciencedirect.com/science/article/pii/S0921452609014379, https://doi.org/10.1016/j.physb.2009.11.071.